

## Journal Pre-proofs

Development of a fine-resolution snow depth product based on the snow cover probability for the Tibetan Plateau: Validation and spatial-temporal analyses

Dajiang Yan, Ning Ma, Yinsheng Zhang

PII: S0022-1694(21)01077-5  
DOI: <https://doi.org/10.1016/j.jhydrol.2021.127027>  
Reference: HYDROL 127027

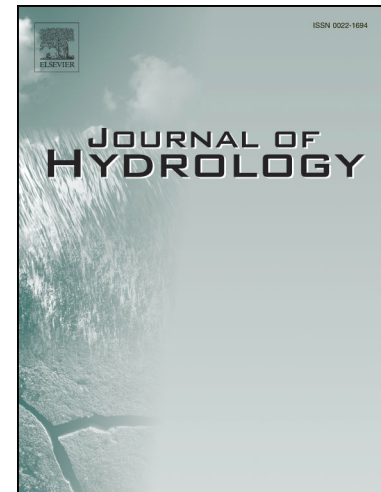
To appear in: *Journal of Hydrology*

Received Date: 13 April 2021  
Revised Date: 26 September 2021  
Accepted Date: 28 September 2021

Please cite this article as: Yan, D., Ma, N., Zhang, Y., Development of a fine-resolution snow depth product based on the snow cover probability for the Tibetan Plateau: Validation and spatial-temporal analyses, *Journal of Hydrology* (2021), doi: <https://doi.org/10.1016/j.jhydrol.2021.127027>

This is a PDF file of an article that has undergone enhancements after acceptance, such as the addition of a cover page and metadata, and formatting for readability, but it is not yet the definitive version of record. This version will undergo additional copyediting, typesetting and review before it is published in its final form, but we are providing this version to give early visibility of the article. Please note that, during the production process, errors may be discovered which could affect the content, and all legal disclaimers that apply to the journal pertain.

© 2021 Elsevier B.V. All rights reserved.



1           **Development of a fine-resolution snow depth product based on**  
2           **the snow cover probability for the Tibetan Plateau: Validation and**  
3                           **spatial-temporal analyses**

4

5                           Dajiang Yan<sup>a,e</sup>, Ning Ma<sup>b\*</sup>, Yinsheng Zhang<sup>a,c,d\*</sup>

6

7           *a State Key Laboratory of Tibetan Plateau Earth System and Resources Environment,*

8           *Institute of Tibetan Plateau Research, Chinese Academy of Sciences, Beijing, China*

9           *b Key Laboratory of Water Cycle and Related Land Surface Processes, Institute of*

10          *Geographic Sciences and Natural Resources Research, Chinese Academy of Sciences,*

11          *Beijing, China*

12          *c CAS Center for Excellence in Tibetan Plateau Earth Sciences, Beijing, China*

13          *d China-Pakistan Joint Research Center on Earth Sciences, CAS-HEC, Islamabad,*

14          *Pakistan*

15          *e University of Chinese Academy of Sciences, Beijing, China*

16

17

18

19          \*Corresponding authors:

20          Ning Ma (Email: ningma@igsnr.ac.cn)

21          Yinsheng Zhang (Email: yszhang@itpcas.ac.cn)

22 **Abstract:** Accurate remotely sensed snow depth (SD) data are essential for monitoring  
23 and modeling hydrological processes in cold regions. While the available passive  
24 microwave SD data have been widely used by the community, the coarse spatial  
25 resolution (typically at  $0.25^\circ$ ) of these data impedes the explicit representation of the  
26 hydrological processes in snow-dominated regions, especially in mountainous regions  
27 with complex terrain. To improve the spatial resolution and quality of passive  
28 microwave SD data for the Tibetan Plateau (TP), we develop a spatial-temporal  
29 downscaling method to produce a 19-year, daily  $0.05^\circ$  SD product by combining the  
30 existing high temporal resolution daily SD data and the high spatial resolution 8-day  
31 cloud-free Moderate Resolution Imaging Spectroradiometer (MODIS)-based snow  
32 cover probability (SCP) data, the latter of which were produced using an advanced  
33 temporal filter algorithm. Validations against the observed SD data from 92  
34 meteorological stations suggest that the newly-developed  $0.05^\circ$  SD product greatly  
35 improves upon the original  $0.25^\circ$  version. Based on this  $0.05^\circ$  SD product, we found  
36 that higher SD values are mainly distributed on the southeastern and eastern TP as well  
37 as the Himalaya and Karakoram, while much lower SD values occur on the inner TP.  
38 During 2000–2018, the TP-averaged annual SD showed a slight ( $p > 0.05$ ) increasing  
39 trend because there were little changes in SD for most grids across the TP. Regarding  
40 different basins within TP, the annual SD during 2000–2018 slightly increased over  
41 most basins except for the Amu Dayra, Ganges, Brahmaputra, and Inner TP, where the  
42 basin-scale SD showed insignificant decreasing tendencies. In general, the spatial-  
43 temporal variations in the SD across the TP were very heterogeneous because SD was

44 affected by multiple climatic factors. The newly-developed 0.05° SD product could  
45 facilitate our understanding of the hydrological processes on the TP through a more  
46 explicit representation of the gridded-based snow water information.

47 **Keywords:** snow depth, downscaling, snow cover probability, Tibetan Plateau

## 48 1. Introduction

49 Snow is a key component of the hydrological cycle and an important indicator of  
50 climate change (Pulliainen et al., 2020; Musselman et al., 2021). It also plays a key role  
51 in the energy balance because of its strong effect on the surface albedo and soil  
52 temperature, thereby modulating the local and regional weather and climate (Henderson  
53 et al., 2018; Jia et al., 2021; You et al., 2020). As the snowpack can store a large amount  
54 of the precipitation that falls during the cold season, it also plays a vital role in the  
55 spring runoff formulation (Barnett et al., 2005; Huninga and AghaKouchaka, 2020),  
56 impacting the downstream agricultural production, which relies on irrigation (Qin et  
57 al., 2020). The snow depth (SD) is the most important variable that describes the  
58 amount of snow for a given region (Kinar and Pomeroy, 2015; Matiu et al., 2021).  
59 Hence, reliable high-quality SD datasets are essential for the above applications related  
60 to the weather and climate, water resource management, and flood monitoring in cold  
61 regions.

62 Several approaches have been extensively used to monitor the SD, including field  
63 observations, land surface modeling, optical remote sensing, and passive microwave  
64 remote sensing. Although meteorological stations can provide accurate SD observation  
65 data for a long time series (Ma et al., 2020; Matiu et al., 2021), the number of stations  
66 in mountainous regions where the snow often occurs remains low (Lundquist et al.,  
67 2019), impeding the understanding of snow dynamics in high-elevation areas. In terms  
68 of the model-based SD estimates, including the lumped conceptual models (e.g., Snow-  
69 17 model) and the physically-based land surface models (e.g., those from the Global

70 Land Data Assimilation System Version 2.1), the uncertainties in the modeling forcing  
71 and the parameters may bring potential errors in regional scale SD estimation, which is  
72 especially true for remote areas where ground observed meteorological data are very  
73 sparse (Bian et al., 2019; Ma et al., 2020). While certain atmospheric reanalysis data,  
74 e.g., the Japanese 55-year Reanalysis (JRA-55), has also assimilated the ground  
75 observations in deriving the gridded SD data, they are typically at the relatively coarse  
76 spatial resolutions with an order of  $0.5^\circ$  or larger (Bian et al., 2020; Orsolini et al., 2019).  
77 Although snow cover information can be extracted from optical remote sensing data  
78 under clear sky conditions (Hall et al., 2007; Bhatti et al., 2016; Zhang et al., 2014), it  
79 is less accurate and more difficult to estimate the SD using the visible and infrared  
80 bands (Dai et al., 2018). With the rapid development of passive remote sensing over the  
81 last four decades, this technique has become widely used for detecting SD information  
82 by taking advantage of the difference in the microwave brightness temperature at  
83 different frequencies regardless of cloud contamination since the 1970s (Chang et al.,  
84 1987; Che et al., 2008; Liang et al., 2015; Tait, 1998; Tedesco et al., 2004). This is  
85 because the deeper the snowpack is, the more positive the microwave energy difference  
86 detected between the horizontally polarized brightness temperatures of the 19 (or 18)  
87 GHz and 37 (or 36) GHz bands (Kelly et al., 2003; Che et al., 2008; Xiao et al., 2018).

88 Previous studies have dedicated much effort to developing and calibrating  
89 numerous SD estimation algorithms for use with passive microwave remote sensing  
90 data. For example, the relationship between the SD and the brightness temperature  
91 gradients of the 18 and 37 GHz bands was used for SD retrievals from Nimbus-7

92 Scanning Multichannel Microwave Radiometer (SMMR) data (Chang et al., 1987).  
93 Considering the effects of forested areas and crystal size on SD estimation, Foster et al.  
94 (1997) presented an algorithm to improve the original one proposed by Chang et al.  
95 (1987) for North America and Eurasia. The Chang et al. (1987) algorithm was also  
96 adjusted to consider several factors influencing the SD retrieval to achieve a more  
97 accurate result in China (Che et al., 2008). This valuable effort produced a Chinese  
98 long-term SD dataset based on this algorithm for the last four decades using three  
99 passive microwave remote sensing sensors, i.e., the SMMR, Special Sensor  
100 Microwave/Imager (SSM/I), and Special Sensor Microwave Imager/Sounder (SSMIS)  
101 (Che et al., 2008; Dai et al., 2015; 2017). Although the microwave remote sensing SD  
102 data allow us to eliminate cloud contamination, its coarse spatial resolution (mostly at  
103  $0.25^\circ$ ) is too coarse to capture the fine-scale characteristics of SD, which is especially  
104 true in mountainous areas with a complex terrain. In addition, the coarse resolution of  
105 such SD products is not adequate for hydrological modeling studies in small watersheds  
106 where the runoff is often simulated at the kilometer scale.

107 The combination of optical snow cover products and microwave snow products is  
108 an important step in developing accurate snow cover and SD products. To mitigate the  
109 uncertainty of microwave remote sensing snow products (e.g., SD and snow water  
110 equivalent) due to its low spatial resolution, it may be preferable to blend the existing  
111 coarse resolution microwave remote sensing SD products and other auxiliary datasets  
112 with higher spatial resolutions to improve the spatial resolution of the SD product. To  
113 this end, various types of snow cover information, e.g., binarized snow cover, fractional

114 snow cover, and annual snow cover duration, usually have much higher spatial  
115 resolutions and thus are widely used to enhance passive microwave snow products (Gao  
116 et al., 2010; Tang et al., 2016; Huang et al., 2016; Dai et al., 2018; Wei et al., 2021).

117 The three main factors derived from the optical-based snow cover information  
118 were used to enhance the coarse resolution microwave SD and snow water equivalent  
119 datasets. First, a binarized snow cover image was used. Gao et al. (2010) redistributed  
120 the snow water equivalent information using the number of snow-covered pixels from  
121 the Moderate Resolution Imaging Spectroradiometer (MODIS) data in a passive  
122 microwave pixel. However, a binarized snow cover image classified using a threshold  
123 tends to underestimate patchy snow cover information to a large extent (Zhang et al.,  
124 2019). Thus, compared to the binarized snow cover, the fractional snow cover should  
125 be given priority to enhance the coarse resolution microwave SD. Second, the spatial  
126 information about the daily fractional snow cover was used. Tang et al. (2016) used a  
127 daily fractional snow cover product to enhance the daily microwave SD data based on  
128 the strong relationship between these two snow parameters. By combining ground  
129 emissivity, land surface temperature, and fractional snow cover, the SD data was further  
130 improved using a novel spatial dynamic method with a higher spatial resolution on the  
131 TP (Dai et al., 2018). However, the accuracy of the daily snow cover product is largely  
132 affected by cloud cover (Zhang et al., 2019). Third, the annual snow cover duration was  
133 used (Mhaweji et al., 2014; Huang et al., 2016; Wang et al., 2019; Wei et al., 2021)  
134 because there is a strong relationship between the snow cover duration and the SD  
135 during a given year. The annual snow cover duration obtained from MODIS data was

136 introduced to redistribute the microwave snow water equivalent data (Mhaweji et al.,  
137 2014) and the SD data (Huang et al., 2016). The relationships between the SD and  
138 several factors (e.g., longitude, latitude, terrain, and snow cover duration) were built  
139 using multi-factor regression models in order to reconstruct the high-resolution SD  
140 products (Wang et al., 2019; Wei et al., 2021). However, using the annual snow cover  
141 duration to reconstruct the daily passive microwave SD pixels is problematic because  
142 of the temporal difference.

143 While progress in downscaling the SD (snow water equivalent) has been made by  
144 taking advantage of more factors, less attention has been paid to enhancing the SD  
145 product by taking advantage of the high spatial resolution MODIS snow cover  
146 probability (SCP) product in previous studies. In short, neither the annual snow cover  
147 duration nor the daily snow cover product, e.g., the binarized snow cover and fractional  
148 snow cover, are suitable for use as a downscaling factor to produce SD datasets with  
149 high temporal-spatial resolutions. The utilization of the MODIS SCP information  
150 during several days can provide new opportunities, thereby improving the spatial  
151 resolution of the passive microwave SD data.

152 With an average altitude higher than 4000 m above sea level (a.s.l.), the Tibetan  
153 Plateau (TP) is the source region of several major Asian rivers, including the Indus,  
154 Ganges, Brahmaputra, Salween, Mekong, Yellow, and Yangtze rivers (Fig. 1), which  
155 is therefore known as the Asian Water Tower (Immerzeel et al., 2010). In this context,  
156 snow is extremely important because it is one of the key water resources that supply  
157 more than 1.6 billion people downstream in China, India, Pakistan, Nepal, Bhutan, and

158 Bangladesh (Immerzeel et al., 2020). However, in-situ observations of snow  
159 information are particularly sparse on the TP because of its complex terrain and harsh  
160 climate (Ma et al., 2020). For this reason, satellite-observed SD products for the TP  
161 have attracted increasing attention because of their ability to estimate the snow water  
162 resources in this inaccessible region with formidable natural conditions (Tang et al.,  
163 2016; Xiong et al., 2017; Zhang and Ma, 2018). However, the development of high-  
164 resolution (both spatially and temporally) remote sensing SD data in the Tibetan Plateau  
165 is challenging because of its heterogeneous landscape and scarce ground observations  
166 (Bian et al., 2019; Orsolini et al., 2019). Having recognized this need, the objectives of  
167 this study are (i) to develop a spatiotemporal downscaling method by taking advantage  
168 of the spatial information of the MODIS SCP and the temporal information of the  
169 passive microwave SD during an 8-day period to produce a finer resolution (i.e.,  $0.05^\circ$ )  
170 SD product across the TP; (ii) to determine whether the accuracy of this newly-  
171 developed  $0.05^\circ$  SD product is better than that of the previous coarse-resolution SD  
172 dataset; and (iii) to investigate the spatial and temporal variations in SD over TP during  
173 the last two decades.

174

## 175 **2 Data**

### 176 **2.1 Fractional snow cover and clear index**

177 The MODIS snow cover data version 006 from 2000 to 2018 from the Terra  
178 (MOD10C1) and Aqua (MYD10C1) satellites were downloaded (accessible from the  
179 National Snow and Ice Data Center (NSIDC), <http://nsidc.org>). The spatial and

180 temporal resolutions are 0.05° and daily, respectively (Hall et al., 2002). Both datasets  
 181 are comprised of three sub-datasets, i.e., the fractional snow cover (FSC), cloud  
 182 obscuration percentage, and clear index (CI) data, ranging from 0% to 100%. Each sub-  
 183 dataset of the MODIS snow cover data includes the following categories: lake ice,  
 184 inland water, ocean, cloud obscured water, data not mapped, and data filled (Table 1).  
 185 Because lake ice, inland water, ocean, and cloud obscured water have no snow cover  
 186 information, these variables were reclassified to 100% in the clear index data. The data  
 187 that were not mapped and the filled data were considered as cloud cover, so they were  
 188 reclassified to 0% in clear index data. The FSC and CI were calculated as follows (Hall  
 189 et al., 1995; Salomonson et al., 2006):

$$190 \quad FSC_{Terra} = 1.45 \times \frac{\rho_{Green} - \rho_{SWIR1}}{\rho_{Green} + \rho_{SWIR1}} - 0.01, \quad (1)$$

191  
 192 where  $FSC_{Terra}$  is the fractional snow cover obtained using the MODIS Terra  
 193 instrument;  $\rho_{Green}$  is the reflectance of the green band; and  $\rho_{SWIR1}$  is the reflectance  
 194 of the SWIR1 band.

$$195 \quad FSC_{Aqua} = 1.91 \times \frac{\rho_{Green} - \rho_{SWIR2}}{\rho_{Green} + \rho_{SWIR2}} - 0.64, \quad (2)$$

196  
 197 where  $FSC_{Aqua}$  is the fractional snow cover obtained using the MODIS Aqua instrument;  
 198  $\rho_{Green}$  is the reflectance of the green band; and  $\rho_{SWIR2}$  is the reflectance of the  
 199 SWIR2 band.

200

$$CI = 1 - FCC, \quad (3)$$

201 where CI is the daily clear index data; and FCC is the daily fractional cloud cover.

202

## 203 **2.2 Gridded SD product**

204 The long-term daily, 0.25° SD dataset from 2000 to 2018 was downloaded from the  
205 National Tibetan Plateau Data Center (<https://data.tpdc.ac.cn/zh-hans/>). This dataset  
206 was obtained by the SMMR, SSM/I, and SSMI/S (Che et al., 2008; Che, 2015; Dai et  
207 al., 2015; 2017). To improve the consistency of the passive microwave remote sensing  
208 data derived from the various sensors, the brightness temperature data derived from  
209 these instruments (SMMR, SSM/I, and SSMI/S) were cross-calibrated (Dai et al., 2015).  
210 This SD dataset has long been regarded as the most accurate snow depth estimation for  
211 China and thus has been widely used not only in previous studies related to SD  
212 downscaling (Huang et al., 2016; Tang et al., 2016; Wei et al., 2021) but also in  
213 understanding the effects of snow changes on regional runoff (Xu et al., 2009) and that  
214 on vegetation dynamics (Yu et al., 2013).

215

## 216 **2.3 Ground measured SD data from meteorological stations**

217 The daily SD data during 2000-2010 observed at 92 meteorological stations (Fig.  
218 1) of the China Meteorological Administration were used as the “ground-truth” values  
219 for assessing the accuracy of the gridded SD product (Wang and Wan, 2018). With  
220 elevations ranging from 1000 to 4800 m above sea level, most meteorological stations

221 are located on the southern and eastern parts of the TP. The in-situ SD measurements  
222 are the most accurate record of the SD, and therefore, they are widely used for  
223 evaluating not only satellite-based SD products (Tang et al., 2016) but also the snow  
224 products in reanalysis over the TP (Orsolini et al., 2019).

225

### 226 **3. Method**

#### 227 **3.1 Definition of the snow hydrological year**

228 According to the seasonal cycle of the SD in TP, the lowest monthly mean SD  
229 occurs in September over the TP. Therefore, the snow year was defined as September  
230 1 to August 31 of the following year. For example, the snow year of 2000 was from  
231 September 1 of 2000 to August 31 of 2001. It should be noted that all analyses in the  
232 present study are based on the snow year instead of the calendar year.

233

#### 234 **3.2 Cloud removal method for estimating the spatial probability of the snow cover**

235 Cloud contamination of optical remote sensing products greatly limits the usage of  
236 daily MODIS snow cover datasets. To remove the clouds from the original MODIS  
237 snow cover product, the ratio of the number of snow pixels to the number of cloud-free  
238 pixels during a 15-day period was used to estimate the spatial probability of the snow  
239 cover by combining the regional snowline and an elevation zone with a 100 m interval  
240 (Li et al., 2017). However, the snow pixels were identified via binarization processing  
241 of the Normalized Difference Snow Index (NDSI) image data, with a specific threshold  
242 on the regional scale, which causes uncertainties in estimating the area of the snow

243 cover (Zhang et al., 2019). To achieve a more accurate spatial probability of snow, the  
 244 binary snow images with snow pixels and non-snow pixels were replaced by the FSC  
 245 images in this study. Similarly, the binary cloud-free images with cloud pixels and non-  
 246 cloud pixels were replaced by the clear index (CI) images.

247 The ratio of the sum of the fractional snow cover ( $FSC_{sum}$ ) data to the sum of the  
 248 clear index ( $CI_{sum}$ ) data during a period is an improved method for estimating the spatial  
 249 probability of the snow cover, which makes full use of the snow cover and cloud  
 250 information from the original MODIS snow product. The new advanced SCP dataset  
 251 was generated by combining MODIS Terra and Aqua data for 2002–2018 at a spatial  
 252 resolution of  $0.05^\circ$  over the entire TP. During 2000–2001, only the MODIS Terra data  
 253 were used because Aqua is not available. Detailed descriptions of the three steps of the  
 254 new method are provided below (Figs. 2 & 3).

255 **Step 1:** The sum of FSC and the sum of the clear index during an 8-day period for  
 256 both the daily MODIS Terra and MODIS aqua datasets covering each pixel of the entire  
 257 TP was calculated as follows:

$$CI_{sum} = \sum_{i=1}^n CI_i, \quad (4)$$

where  $CI_{sum}$  is the sum of the daily clear index data during an 8-day period.

$$FSC_{sum} = \sum_{i=1}^n FSC_i, \quad (5)$$

258 where  $FSC_{sum}$  is the sum of the fractional snow cover from the original daily MODIS  
 259 snow cover product during an 8-day period.

260 **Step 2:** If the sum of the daily clear index for a pixel was higher than 0 within the  
 261 8-day period, the spatial probability of snow cover in this pixel was estimated as

262 follows:

$$SCP = \frac{FSC_{sum}}{CI_{sum}} = \frac{\sum_{i=1}^n FSC_i}{\sum_{i=1}^n CI_i}, \quad (6)$$

263 where SCP is the 8-day cloud-free snow cover probability.

264 The above two steps effectively remove most of the clouds in the original MODIS  
 265 snow cover product during an 8-day period. If CI is zero in all of the pixels from the  
 266 Terra and Aqua sensors during this period, a backup forecasting method was used in  
 267 the next step.

268 **Step 3:** If the pixel was completely (100%) covered by clouds during the entire 8-  
 269 day period, the spatial probability of snow cover was estimated using the cloud-free  
 270 spatial probability of snow cover for the preceding 8-day period (PSCP) and that of the  
 271 following 8-day period (FSCP) as follows:

$$SCP = \left\{ \begin{array}{l} (PSCP + FSCP)/2, \text{ PSCP and FSCP are available} \\ PSCP, \text{ FSCP is not available} \\ FSCP, \text{ PSCP is not available} \end{array} \right\}. \quad (7)$$

272 Using the above three steps, we were able to estimate the SCP regardless of almost all  
 273 of the cloud cover, with a time span of 24 days.

274 The results of the SCP estimation are shown in [Fig. 4](#). The SCP could be easily  
 275 estimated using Step 2 when the sum of the CI in the pixels is greater than 0 during an  
 276 8-day period. When a small part of the pixels is fully covered by clouds for all time  
 277 within a given period, the preceding and the subsequent 8-day cloud-free SCP data for  
 278 the same pixels estimated using Step 3 are employed to fill such a gap. As a result, an  
 279 8-day SCP dataset without cloud cover could be produced using the above three steps.

280

### 281 **3.3 Relationship between passive microwave SD product and SCP**

282 Snow cover information with a high spatial resolution is a key factor and has been  
283 widely used as a spatial weight when redistributing passive microwave SD pixels in  
284 previous studies. These studies identified a positive correlation between the FSC and  
285 SD over the TP (Tang et al., 2016; Dai et al., 2018), indicating that the FSC can be used  
286 to determine the detailed spatial information for the passive microwave SD pixels.  
287 Therefore, the SCP generated from the FSC has the potential ability to redistribute  
288 passive microwave SD pixels.

289 To illustrate, we selected two typical regions with a large amount of snow in the  
290 TP. The 8-day mean SD and SCP values from 300 grid points during winter 2000 were  
291 randomly extracted for the western TP and for the southeastern TP, which are the two  
292 main snow-covered regions on the TP. Thus, a total of 600 grid points were sampled to  
293 test the relationship between the SD and SCP in the cold season. A simple linear  
294 regression model was then established based on these collected SCP and SD data. In  
295 each region, we found a significant positive relationship between the SD and SCP, as  
296 can be seen from the R values of 0.74 for the western TP and 0.88 for the southeastern  
297 TP ( $p < 0.001$  in both cases) (Fig. 5). Thus, the SCP was determined to be an appropriate  
298 factor for downscaling the coarse-resolution SD data used in this study.

299

### 300 **3.4 Downscaling algorithms**

#### 301 **3.4.1 Spatial downscaling algorithm**

302 The above analysis suggests that a higher SCP value may indicate a higher SD value.  
 303 Therefore, it is reasonable to use the SCP derived from the FSC product to improve the  
 304 spatial resolution of the SD grids. To maintain the same temporal resolution for the SD  
 305 and SCP, the total SD ( $SD_{sum}$ ) during an 8-day period dataset was produced by summing  
 306 the daily SD data for each 8-day period by:

$$SD_{sum} = \sum_{i=1}^8 SD_i, \quad (8)$$

308  
 309 The area of a  $0.25^\circ$  passive microwave SD pixel is 25 times that of an  $0.05^\circ$  SCP  
 310 pixel. Thus, each  $0.25^\circ$  SD pixel was equally divided into 25 subpixels by taking into  
 311 consideration the spatial weight derived from the  $0.05^\circ$  SCP in the same location.  
 312 Dividing the sum of the  $0.05^\circ$  SCP in the extent of the  $0.25^\circ$  SD pixel by each  $0.05^\circ$   
 313 SCP pixel is an effective way to estimate each spatial weight that is used to redistribute  
 314 the  $0.25^\circ$  SD pixels. In this case, the 8-day  $SD_{sum}$  grids must be multiplied by 25 before  
 315 multiplying by the subpixel-level spatial weight value. In this way, an 8-day  $SD_{sum}$   
 316 dataset with the  $0.05^\circ$  resolution subpixel spatial information was produced for 2000–  
 317 2018 over the TP (Fig. 6). The equations of spatial downscaling algorithm are as  
 318 follows:

$$WS = \frac{SCP_j}{\sum_{j=1}^{25} SCP_j} = \begin{bmatrix} W_{11} & \cdots & W_{15} \\ \vdots & \ddots & \vdots \\ W_{51} & \cdots & W_{55} \end{bmatrix}, \quad (9)$$

319

$$(SD_{sum})_{sub} = 25 \times SD_{sum} \times W_s = \begin{bmatrix} 25 \times SD_{sum} \times W_{11} & \cdots & 25 \times SD_{sum} \times W_{15} \\ \vdots & \ddots & \vdots \\ 25 \times SD_{sum} \times W_{51} & \cdots & 25 \times SD_{sum} \times W_{55} \end{bmatrix}, \quad (10)$$

320

321 where  $(SD_{sum})_{sub}$  is the sum of the subpixel snow depth at  $0.05^\circ$  during an 8-day period,322  $SD_i$  is the snow depth on the  $i$ th day during an 8-day period ( $1 \leq i \leq 8$ ),  $W_s$  is the spatial323 weight for redistributing the passive microwave snow depth pixel, and  $SCP_j$  is the snow324 cover probability in the  $j$ th pixel in the area of each  $0.25^\circ$  snow depth pixel ( $1 \leq j \leq 25$ ).

325

326 **3.4.2 Temporal downscaling algorithm**

327 In the process of downscaling the passive microwave SD, the advantage of its high

328 temporal resolution has long been disregarded in previous studies. Using the ratio of

329 daily SD to the 8-day  $SD_{sum}$ , the daily temporal weight can be calculated to improve330 the temporal resolution of the 8-day  $SD_{sum}$  dataset containing subpixel spatial

331 information. A subpixel SD dataset with a daily temporal resolution during 2000–2018

332 in the study region was produced by multiplying the 8-day  $SD_{sum}$  subpixel dataset and

333 each daily temporal weight. The flowchart of the temporal downscaling algorithm is

334 shown in Fig. 7, and the equations are as follows:

335

$$Wt = \frac{SD_i}{\sum_{i=1}^8 SD_i} = \left[ \frac{SD_1}{\sum_{i=1}^8 SD_i} \quad \cdots \quad \frac{SD_8}{\sum_{i=1}^8 SD_i} \right], \quad (11)$$

$$\begin{aligned} (SD_i)_{sub} &= (SD_{sum})_{sub} \times Wt = \\ &[(SD_{sum})_{sub} \times W_1 \quad \cdots \quad (SD_{sum})_{sub} \times W_8] = \end{aligned} \quad (12)$$

$$\left[ (SD_{sum})_{sub} \times \frac{SD_1}{\sum_{i=1}^8 SD_i} \quad \dots \quad (SD_{sum})_{sub} \times \frac{SD_8}{\sum_{i=1}^8 SD_i} \right],$$

336

337 where  $(SD_i)_{sub}$  is the subpixel daily snow depth on the  $i$ th day,  $(SD_{sum})_{sub}$  is the sum of  
 338 the subpixel snow depth during an 8-day period,  $W_t$  is the temporal weight, and  $SD_i$  is  
 339 the snow depth on the  $i$ th day during an 8-day period ( $1 \leq i \leq 8$ ).

340

### 341 3.5 Statistical metrics for assessing the SD product

342 The daily in-situ SD data measured at 92 meteorological stations of the China  
 343 Meteorological Administration (CMA) were used to evaluate the accuracy of the new  
 344 daily  $0.05^\circ$  SD product and the original  $0.25^\circ$  one for 2000–2010. For each product, the  
 345 SD value of the grid in which the station is located was compared against that observed  
 346 by the meteorological stations. Based on the elevations of the stations, the comparisons  
 347 were also aggregated into four elevation zones with a 1000 m interval. The root-mean-  
 348 square-error (RMSE) and the mean-absolute-error (MAE) values were calculated to  
 349 quantitatively evaluate the accuracy of these two products, i.e.,

350

$$RMSE = \sqrt{\frac{1}{n} \sum_{i=1}^n (x_i - y_i)^2}, \quad (13)$$

$$MAE = \frac{1}{n} \sum_{i=1}^n |x_i - y_i|, \quad (14)$$

351

352 where  $x_i$  is the  $i$ th in-situ snow depth value, and  $y_i$  is the  $i$ th passive microwave snow  
 353 depth value.

354

## 355 4. Results

### 356 4.1 Validations of the original 0.25° SD product and the new 0.05° SD product

357 [Fig. 8](#) shows the validation results of the new 0.05° and the original 0.25° SD data  
358 using the ground measured SD data. As seen, the RMSE and MAE values from the  
359 former are much smaller than those from the latter, indicating a significant  
360 improvement in the 0.05° SD product across the TP. For all 92 stations, the mean RMSE  
361 and MAE values of the new 0.05° SD product are 1.54 and 0.67 cm d<sup>-1</sup>, respectively.  
362 The spatial distribution for the RMSE and MAE of two SD products ([Fig. 9](#)) shows that  
363 the improvement of new SD estimates is more obvious in the eastern part of TP. For  
364 certain stations in the southeastern TP, however, the difference in the accuracy of these  
365 two products seems not obvious. This may be attributed to the inherent larger error in  
366 the original 0.25° SD product in this area where numerous forests are found.

367 Regarding the stations in different elevation zones ([Table 2](#)), the RMSE values of  
368 the new 0.05° SD product are all lower than those of the original 0.25° SD product.  
369 This is also true for the MAE values. The improvement is most obvious in the 3000–  
370 4000 m a.s.l. elevation zone, in which the RMSE decreases from 3.22 to 2.30 m d<sup>-1</sup>  
371 ([Table 2](#)). The above validation suggests that our newly-developed SD product with a  
372 higher spatial resolution outperforms the original 0.25° SD product regarding the  
373 accuracy.

374

### 375 4.2 Spatial pattern of the SD over the TP from the new and original SD products

376 [Fig.10](#) presents the spatial characteristics of the multiyear (2000–2018) mean SD  
377 from the new 0.05° and original 0.25° SD products over the TP. As can be seen, the  
378 two SD products exhibit similar spatial distribution characteristics. However, the new  
379 SD product with a 0.05° spatial resolution captures much more detailed information  
380 and provides more heterogeneous spatial distribution patterns compared to the original  
381 version. This is because the former assimilates the much spatial information of the SCP,  
382 the latter of which was derived from the MODIS with a high spatial resolution. The  
383 difference between these two products is most obvious in the snow-dominated regions,  
384 i.e., the southeastern TP as well as the Himalaya and Karakoram.

385 To further illustrate the strength of the new 0.05° SD product at the monthly scale,  
386 [Figs. 11 & S2](#) further illustrate the spatial distribution of the multiyear (2000–2018)  
387 mean monthly SD across TP. As seen, a more explicit spatial pattern of SD across TP  
388 could be detected every month by the new 0.05° SD product. With this new 0.05° SD  
389 product, we could describe the spatial characteristic of SD in a more detailed manner.  
390 On the monthly scale, the spatial pattern of the multiyear (2000–2018) average SD over  
391 the TP differs significantly in the cold and warm seasons ([Figs. 11 & S2](#)). During the  
392 cold season, the large SD values mainly occur on the northwestern and southeastern  
393 TP, while the SD values in the inner TP are much smaller. During the warm season,  
394 there is little snow on most parts of the TP, except for the high-elevation areas of  
395 Karakorum, Kunlun, Himalaya, and Pamir, where a certain amount of snow still exists  
396 during the warm season. Note that although the 0.05° SD product has an improved  
397 spatial resolution, it may be less capable of presenting the spatial information about the

398 snowpack in summer. This is mainly because the microwave data cannot efficiently  
399 detect the SD in regions with shallow SD values.

400

#### 401 **4.3 Seasonal cycle of the SD over the TP and its basins**

402 The multiyear mean monthly SD averaged over the entire TP increases rapidly from  
403 September to January, leading to a peak monthly value of 3.54 cm mo<sup>-1</sup> (Fig. 12m).  
404 This is followed by a gradual decrease until September. In general, the rate of increase  
405 of the monthly SD during September-January is obviously faster than the rate of  
406 decrease of the monthly SD during January-September, which suggests that the  
407 duration of the snow melting period is likely longer than the snow accumulation period  
408 over the TP.

409 Figs. 12a–l illustrate the seasonal cycle of the SD in 12 basins within the TP. In  
410 general, the lowest monthly SD occurs in July or August over the basins in the eastern  
411 TP, but for the basins in the western and inner TP, the lowest monthly SD occurs in  
412 September. For most basins that are influenced by the Asian Monsoon, the maximum  
413 monthly SD occurs in December or January. However, for the Amu Dayra, Indus, and  
414 Ganges, which are obviously impacted by the westerlies, the SD is large until April.  
415 The above analysis highlights that the monsoon and westerlies play important roles in  
416 controlling the intra-annual SD variations in the different basins across TP.

417

#### 418 **4.4 Trends in the SD over the entire TP and its basins**

419 Fig. 13a shows the spatial pattern of the trends (2000–2018) in annual SD across

420 the TP derived from the new 0.05° product. The SD increased significantly in some  
421 parts of the Tarim, upper Yangtze, Yellow, and Mekong River basins and the northern  
422 Himalayas, but it decreased significantly in some parts of the inner TP, eastern  
423 Brahmaputra, and the southern Himalayas. However, in most parts of TP, the trends of  
424 the annual SD were not significant during 2000–2018 (Fig. 13b). To further illustrate  
425 the strength of the new high-resolution SD data, we also show the spatial pattern of the  
426 trends in annual SD derived from the 0.25° product in Fig. S2. Although the spatial  
427 pattern of the linear trends derived from the 0.25° version is overall similar to those  
428 from the 0.05° product, the new data obviously provide a more explicit representation  
429 of the changes in SD across TP. Therefore, it is suggested that our newly-developed SD  
430 data could serve as a useful tool for investigating the spatial and temporal variations in  
431 snow over TP.

432 When averaged over the entire TP, the annual SD increased slightly with a rate of  
433 0.005 cm yr<sup>-1</sup> ( $p > 0.05$ ) during 2000–2018 (Fig. 14m). The annual SD generally  
434 increased during 2000–2008 and 2017–2018, and it decreased overall during 2008–  
435 2017. It should be highlighted that the trend in the SD depends highly on the temporal  
436 period analyzed since there was a sudden jump in the SD in 2018 (which is also the  
437 largest annual SD during these 19 years). For this reason, the trend in TP-averaged  
438 annual SD became a slight decreasing one with a value of  $-0.009$  cm yr<sup>-1</sup> ( $p > 0.05$ )  
439 during 2000–2017 (Fig. S3m).

440 Figs. 14a–l also illustrate the linear trends in the annual SD during 2000–2018 for  
441 12 basins within the TP. The annual SD increased in most of the basins in the TP, except

442 the Amu Dayra, Ganges, Brahmaputra, and Inner TP, in which the annual SD decreased  
443 to some extent. However, the trends are mostly insignificant, except for that of the  
444 Tarim Basin, in which the annual SD increased significantly at a rate of  $0.05 \text{ cm yr}^{-1}$   
445 ( $p < 0.05$ ) during the 19-year study period. When switching to the period of 2000–2017  
446 (Fig. S3), trends in basin-scale annual SD change to some extent. In particular, trends  
447 in Indus, Salween, Mekon, Yangtze, and Qaidam become decreasing, though such  
448 trends are still not statistically significant.

449

## 450 5. Discussions

451 Although the SD dataset was improved, with a better resolution of  $0.05^\circ$ , the error  
452 of the representativeness is inevitable when validating pixel-based SD products based  
453 on ground-based SD measurements. This is because a sample point is less capable of  
454 representing a pixel, especially in regions with a heterogeneous underlying surface  
455 (Xiao et al., 2018). To improve the reliability of the validation results of the SD  
456 products derived from remote sensing satellites across the entire TP, progress should  
457 be made not only in developing downscaling algorithms but also in enhancing advanced  
458 sensors.

459 Although the SD retrieval method has been calibrated and developed using several  
460 versions (Chang et al., 1987; Foster et al., 1997; Che et al., 2008; Jiang et al., 2014),  
461 accurate knowledge of the physical properties of the snowpack, e.g., snow temperature,  
462 snow density, snow grain size, and snow water content, is not explicitly and  
463 comprehensively considered used in most of the retrieval methods using the passive

464 microwave remote sensing data (Dietz et al., 2012). Thus, in future studies, more  
465 dynamic SD retrieval methods should be developed to consider the various effects of  
466 these physical properties to improve the accuracy of the original SD products derived  
467 from passive microwave brightness temperature data.

468 It is more suitable to use passive microwave remote sensing to estimate the snow  
469 water equivalent rather than the SD. This is mainly because the microwave brightness  
470 temperature of the snowpack is affected by both SD and snow density (Kelly et al.,  
471 2003). However, most of these algorithms involved the relationship between the SD  
472 value and the passive microwave brightness temperature (Chang et al., 1987; Foster et  
473 al., 1997; Che et al., 2008; Jiang et al., 2014). Therefore, it is believed that these  
474 algorithms may also be appropriate for estimating the snow water equivalent after slight  
475 modifications. In this case, more attention should be paid to building more snow water  
476 equivalent measurement sites because of the limited global samples available for  
477 validation.

478 Several factors may impact the trend of the snow parameters over the TP to some  
479 extent, such as the study area and study period. The effects of the size of the TP  
480 coverage on the trends of the snow parameters have long been disregarded. For example,  
481 the TP's extent in China is less than the entire TP region in this study (Zhang et al.,  
482 2013). It is worthwhile to highlight the SD in certain areas of the western TP (e.g., the  
483 Karakoram) is higher than other parts of the TP, thus making them a significant  
484 contributor to the trend in the TP-averaged annual SD. A good example of this is that  
485 the seasonal cycle of the SD over the entire TP is influenced by the high SD values in

486 the western TP to a large extent, which is especially true in summer. Additionally, the  
487 trend in the annual SD is also very sensitive to the length of the study period, as can be  
488 seen from the comparisons between Fig. 14 and Fig. S3. Although the SD in most of  
489 the basins in the TP increased slightly from 2000 to 2018, it decreased slightly from  
490 2000 to 2017. Different trends during these two different periods are also true for the  
491 TP-averaged annual SD, though both trends are not statically significant.

492

## 493 **6. Conclusions**

494 By combining a high temporal resolution passive microwave SD dataset with a high  
495 spatial resolution cloud-free SCP dataset, this study developed a spatial-temporal  
496 downscaling method to successfully downscale the  $0.25^\circ$  SD dataset to a  $0.05^\circ$  SD  
497 product for the TP during 2000–2018. The validation against 92 ground meteorological  
498 stations demonstrates that the new  $0.05^\circ$  SD product significantly improves upon the  
499 original  $0.25^\circ$  version. While the present study only focuses on the TP, the spatial-  
500 temporal downscaling method proposed here could be applied to other snow-dominated  
501 regions (e.g., the high latitudes) to produce new SD data with an improved spatial  
502 resolution.

503 Based on the new  $0.05^\circ$  SD product, we found that SD is typically higher in the  
504 southeastern TP as well as the Himalaya and Karakoram, while the lowest SD value  
505 occurs mainly in the inner TP. For the seasonal cycle of SD, the maximum monthly  
506 SD occurs in December or January for most basins that are influenced by the Asian  
507 Monsoon. However, for the Amu Dayra, Indus, and Ganges, which are obviously

508 impacted by the westerlies, the SD is large until April. This indicates that the monsoon  
509 and westerlies play important roles in controlling the intra-annual SD variations  
510 patterns across TP.

511 During 2000–2018, there was no significant trend in annual SD for most parts of  
512 TP. The TP-averaged annual SD showed a slight increasing trend ( $0.005 \text{ cm a}^{-1}$ ,  $p >$   
513  $0.05$ ). On the basin scale, the annual SD slightly decreased in the Amu Dayra, Ganges,  
514 Brahmaputra, and Inner TP, but an opposite trend was observed in the rest of the basins  
515 within TP. It should be noted that the trends reported here depend greatly on the study  
516 period since there was a sudden jump in the SD for the last year (i.e., 2018) we analyzed.  
517 However, trends are still not statistically significant after removing this year's data.

518 The demand for high-resolution remote sensing-based SD datasets can be met to  
519 some extent by the current SD data downscaling algorithms. Therefore, it is believed  
520 that the new fine-resolution SD dataset not only provides an accurate data source for  
521 estimating snow water storage and its variations over the TP, but also presents new  
522 opportunities for hydrological and climatological studies related to the seasonal  
523 snowpack. More importantly, the response mechanism of SD to ongoing climate  
524 change on the TP is expected to be clarified in the future by using such an improved  
525 SD dataset.

526

## 527 **Author Contributions**

528 **Dajiang Yan:** Conceptualization, Methodology, Formal analysis, Software,  
529 Investigation, Resources, Data curation, Writing-original draft, Visualization. **Ning Ma:**

530 Investigation, Formal analysis, Writing-original draft, Funding acquisition. **Yinsheng**  
531 **Zhang**: Writing-review & editing, Funding acquisition, Supervision.

532

### 533 **Acknowledgements**

534 This research was funded by the National Key Research and Development Program of  
535 China (2017YFA0603101), the Second Tibetan Plateau Scientific Expedition and  
536 Research Program (2019QZKK0201), the CAS Strategic Priority (A) Research  
537 Program (XDA20060201), the National Natural Science Foundation of China  
538 (41801051), the China-Pakistan Joint Research Center for Earth Science, and the Open  
539 Research Fund Program of the State Key Laboratory of Cryospheric Science,  
540 Northwest Institute of Eco-Environment and Resources, CAS (SKLCS-OP-2020-11).  
541 The fractional snow cover product was acquired from the NSIDC (<http://nsidc.org>). The  
542 0.25° SD dataset was provided by the National Tibetan Plateau Data Center  
543 (<https://doi.org/10.11888/Geogra.tpdc.270194>). The 0.05° SD product is available  
544 upon request from the corresponding authors. The authors thank Prof. Guoqing Zhang  
545 for his helpful suggestions on the manuscript.

546

### 547 **Conflicts of Interest**

548 The authors declare that there are no potential conflicts of interest.

549

### 550 **References**

551 Barnett, T. P., Adam, J. C. & Lettenmaier, D. P. 2005. Potential impacts of a warming

- 552 climate on water availability in snow-dominated regions. *Nature* 438, 303–309.
- 553 Bhatti, A.M.; Koike, T.; Shrestha, M. 2016. Climate change impact assessment on  
554 mountain snow hydrology by water and energy budget-based distributed  
555 hydrological model. *J. Hydrol.* 543, 523–541.
- 556 Bian Q, Xu Z, Zhao L, Zhang Y-F, Zheng HUI, Shi C, Zhang S, Xie C, Yang Z-L  
557 (2019) Evaluation and intercomparison of multiple snow water equivalent  
558 products over the Tibetan Plateau. *J. Hydrometeorol.* 20, 2043-2055.
- 559 Bian, Q., Xu, Z., Zheng, H., Li, K., Liang, J., Fei, W., Shi, C., Zhang, S., Yang, Z.L.,  
560 2020. Multiscale Changes in Snow Over the Tibetan Plateau During 1980–2018  
561 Represented by Reanalysis Data Sets and Satellite Observations. *J. Geophys. Res.*  
562 *Atmos.* 125, e2019JD031914. <https://doi.org/10.1029/2019JD031914>.
- 563 Chang, A., Foster, J., Hall, D., 1987. Nimbus-7 SMMR derived global snow cover  
564 parameters. *Ann. Glaciol.* 9, 39–44.
- 565 Che, T., Xin, L., Jin, R., Armstrong, R., Zhang, T., 2008. Snow depth derived from  
566 passive microwave remote-sensing data in China. *Ann. Glaciol.* 49, 145–154.
- 567 Che, T. 2015. Long-term series of daily snow depth dataset in China (1979-2019).  
568 National Tibetan Plateau Data Center.  
569 <https://doi.org/10.11888/Geogra.tpdc.270194>.
- 570 Dai, L.Y., Che, T., Ding, Y.J. 2015. Inter-calibrating SMMR, SSM/I and SSMI/S data  
571 to improve the consistency of snow-depth products in China. *Remote Sens.* 7(6),  
572 7212-7230.
- 573 Dai, L.Y., Che, T., Ding, Y.J., & Hao, X.H. 2017. Evaluation of snow cover and snow

- 574 depth on the Qinghai-Tibetan Plateau derived from passive microwave remote  
575 sensing. *The Cryosphere*, 11(4), 1933-1948.
- 576 Dai, L., Che, T., Xie, H., Wu, X., 2018. Estimation of Snow Depth over the Qinghai-  
577 Tibetan Plateau Based on AMSR-E and MODIS Data. *Remote Sens.* 10, 1989.  
578 <https://doi.org/10.3390/rs10121989>.
- 579 Dietz, A.J., Kuenzer, C., Gessner, U., Dech, S., 2012. Remote sensing of snow-a  
580 review of available methods. *Int. J. Remote Sens.* 33 (13), 4094–4134.
- 581 Foster, J.L., Chang, A.T.C., Hall, D.K., 1997. Comparison of snow mass estimates from  
582 a prototype passive microwave snow algorithm, a revised algorithm and a snow  
583 depth climatology. *Remote Sens. Environ.* 62(2), 132–142.
- 584 Gao, Y., Xie, H., Lu, N., Yao, T., Liang, T., 2010. Toward advanced daily cloud-free  
585 snow cover and snow water equivalent products from Terra–Aqua MODIS and  
586 Aqua AMSR-E measurements. *J. Hydrol.* 385, 23-35.
- 587 Hall, D. K.; Salomonson, V. V.; Riggs, G. A. 1995. Development of methods for  
588 mapping global snow cover using moderate resolution imaging spectroradiometer  
589 data. *Remote Sens. Environ.* 54(2). [https://doi.org/10.1016/0034-4257\(95\)00137-](https://doi.org/10.1016/0034-4257(95)00137-P)  
590 [P.](https://doi.org/10.1016/0034-4257(95)00137-P)
- 591 Hall, D. K., Riggs, G. A., Salomonson, V. V., Digirolamo, N. E., & Bayr, K. J. 2002.  
592 Modis snow-cover products. *Remote Sens. Environ.* 83(1-2), 181-194.
- 593 Hall, D.K.; Riggs, G.A. 2007. Accuracy assessment of the MODIS snow products.  
594 *Hydrol. Process.* 21, 1534–1547.
- 595 Henderson, G. R., Y. Peings, J. C. Furtado, and P. J. Kushner, 2018: Snow-atmosphere

- 596 coupling in the Northern Hemisphere. *Nat. Clim. Change*, 8, 954-963.
- 597 Huang, X., Deng, J., Ma, X., Wang, Y., Feng, Q., Hao, X., Liang T. 2016.
- 598 Spatiotemporal dynamics of snow cover based on multi-source remote sensing  
599 data in china. *The Cryosphere*, 10(5), 2453-2463.
- 600 Huninga, L.S. and AghaKouchaka, A., 2020. Global snow drought hot spots and  
601 characteristics. *Proc. Natl. Acad. Sci. U. S. A.*, 117(33), 19753-19759.
- 602 Immerzeel, W.W., van Beek, L.P., Bierkens, M.F., 2010. Climate change will affect  
603 the Asian water towers. *Science* 328, 1382-1385.
- 604 Immerzeel, W.W., Lutz, A.F., Andrade, M., Bahl, A., Biemans, H., Bolch, T., Hyde,  
605 S., Brumby, S., Davies, B.J., Elmore, A.C., Emmer, A., Feng, M., Fernandez, A.,  
606 Haritashya, U., Kargel, J.S., Koppes, M., Kraaijenbrink, P.D.A., Kulkarni, A.V.,  
607 Mayewski, P.A., Nepal, S., Pacheco, P., Painter, T.H., Pellicciotti, F., Rajaram,  
608 H., Rupper, S., Sinisalo, A., Shrestha, A.B., Viviroli, D., Wada, Y., Xiao, C., Yao,  
609 T., Baillie, J.E.M., 2020. Importance and vulnerability of the world's water towers.  
610 *Nature* 577, 364-369.
- 611 Jia, X., Zhang, C., Wu, R., Qian, Q., 2021. Influence of Tibetan Plateau autumn snow  
612 cover on interannual variations in spring precipitation over southern China. *Clim.*  
613 *Dynam.*, 56, 767-782.
- 614 Jiang, L., Wang, P., Zhang, L., Yang, H., Yang, J., 2014. Improvement of snow depth  
615 retrieval for FY3B-MWRI in China. *Sci. China Earth Sci.* 57, 1278-1292.
- 616 Kelly, R.E., Chang, A.T., Tsang, L., Foster, J.L., 2003. A prototype AMSR-E global  
617 snow area and snow depth algorithm. *IEEE. T. Geosci. Remote.* 41(2), 230-242.

- 618 Kinar, N.J., Pomeroy, J.W., 2015. Measurement of the physical properties of the  
619 snowpack. *Rev. Geophys.* 53 (2), 481–544.
- 620 Li, X., Fu, W., Shen, H., Huang, C., Zhang, L., 2017. Monitoring snow cover variability  
621 (2000–2014) in the Hengduan Mountains based on cloud-removed MODIS  
622 products with an adaptive spatio-temporal weighted method. *J. Hydrol.* 551, 314-  
623 327.
- 624 Liang, J., Liu, X., Huang, K., Li, X., Shi, X., Chen, Y., Li, J., 2015. Improved snow  
625 depth retrieval by integrating microwave brightness temperature and  
626 visible/infrared reflectance. *Remote Sens. Environ.* 156, 500–509.
- 627 Lundquist, J., Hughes, M., Gutmann, E., Kapnick, S., 2019. Our skill in modeling  
628 mountain rain and snow is bypassing the skill of our observational networks. *Bull.*  
629 *American Meteorol. Soc.*, 100(12), 2473-2490
- 630 Ma, N., Yu, K., Zhang, Y., Zhai, J., Zhang, Y., Zhang, H., 2020. Ground observed  
631 climatology and trend in snow cover phenology across China with consideration  
632 of snow-free breaks. *Clim. Dynam.* 55, 2867-2887.
- 633 Matiu, M., Crespi, A., Bertoldi, G., Carmagnola, C.M., Marty, C., Morin, S., Schöner,  
634 W., Cat Berro, D., Chiogna, G., De Gregorio, L., Kotlarski, S., Majone, B., Resch,  
635 G., Terzago, S., Valt, M., Beozzo, W., Cianfarra, P., Gouttevin, I., Marcolini, G.,  
636 Notarnicola, C., Petitta, M., Scherrer, S.C., Strasser, U., Winkler, M., Zebisch, M.,  
637 Cicogna, A., Cremonini, R., Debernardi, A., Faletto, M., Gaddo, M., Giovannini,  
638 L., Mercalli, L., Soubeyroux, J.-M., Sušnik, A., Trenti, A., Urbani, S., Weilguni,  
639 V., 2021. Observed snow depth trends in the European Alps: 1971 to 2019. *The*

- 640 Cryosphere, 15(3), 1343-1382.
- 641 Mhawej, M., Faour, G., Fayad, A., Shaban, A., 2014. Towards an enhanced method to  
642 map snow cover areas and derive snow-water equivalent in Lebanon. *J. Hydrol.*  
643 513, 274-282.
- 644 Musselman, K.N., Addor, N., Vano, J.A., Molotch, N.P., 2021. Winter melt trends  
645 portend widespread declines in snow water resources. *Nat. Clim. Change*, 11, 418-  
646 424.
- 647 Orsolini, Y., Wegmann, M., Dutra, E., Liu, B., Balsamo, G., Yang, K., de Rosnay, P.,  
648 Zhu, C., Wang, W., Senan, R., Arduini, G., 2019. Evaluation of snow depth and  
649 snow cover over the Tibetan Plateau in global reanalyses using in situ and satellite  
650 remote sensing observations. *The Cryosphere* 13, 2221-2239.
- 651 Pulliainen, J., Luojus, K., Derksen, C., Mudryk, L., Lemmetyinen, J., Salminen, M.,  
652 Ikonen, J., Takala, M., Cohen, J., Smolander, T., Norberg, J., 2020. Patterns and  
653 trends of Northern Hemisphere snow mass from 1980 to 2018. *Nature*, 581(7808),  
654 294-298.
- 655 Qin, Y., Abatzoglou, J.T., Siebert, S., Huning, L.S., AghaKouchak, A., Mankin, J.S.,  
656 Hong, C., Tong, D., Davis, S.J., Mueller, N.D., 2020. Agricultural risks from  
657 changing snowmelt. *Nat. Clim. Change* 10, 459-465.
- 658 Salomonson, V.V.; Appel, I. 2006. Development of the Aqua MODIS NDSI fractional  
659 snow cover algorithm and validation results. *IEEE. Trans. Geosci. Remote* 44,  
660 1747–1756.
- 661 Tait, A., 1998. Estimation of snow water equivalent using passive microwave radiation

- 662 data. *Remote Sens. Environ.* 64, 286–291.
- 663 Tang, Z., Li, H., Wang, J., Liang, J., Li, C., Che, T., Wang X., 2016. Reconstruction of  
664 snow depth over the Tibetan Plateau based on multi-source data. *J. Geo-inf Sci.*,  
665 18 (7):941-950.
- 666 Tedesco, M., Pulliainen, J., Takala, M., Hallikainen, M., Pampaloni, P., 2004. Artificial  
667 neural network-based techniques for the retrieval of SWE and snow depth from  
668 SSM/I data. *Remote Sens. Environ.* 90, 76–85.
- 669 Wang S and Wan G., 2018. Snow depth dataset from station in the Tibetan Plateau  
670 (1961-2013). Cold and Arid Regions Environmental and Engineering Research  
671 Institute, Chinese Academy of Sciences, [http://hdl.pid21.cn/21.86109/casearth.  
672 5c19a5690600cf2a3c557bc2](http://hdl.pid21.cn/21.86109/casearth.5c19a5690600cf2a3c557bc2).
- 673 Wang, Y., Huang, X., Wang, J., Zhou, M., Liang, T., 2019. AMSR2 snow depth  
674 downscaling algorithm based on a multifactor approach over the Tibetan Plateau,  
675 China. *Remote Sens. Environ.* 231. <https://doi.org/10.1016/j.rse.2019.111268>.
- 676 Wei, P., Zhang, T., Zhou, X., Yi, G., Li, J., Wang, N., Wen, B., 2021. Reconstruction  
677 of Snow Depth Data at Moderate Spatial Resolution (1 km) from Remotely Sensed  
678 Snow Data and Multiple Optimized Environmental Factors: A Case Study over  
679 the Qinghai-Tibetan Plateau. *Remote Sens.* 13.  
680 <https://doi.org/10.3390/rs13040657>.
- 681 Xiao, X., Zhang, T., Zhong, X., Shao, W., Li, X., 2018. Support vector regression snow-  
682 depth retrieval algorithm using passive microwave remote sensing data. *Remote  
683 Sens. Environ.* 210, 48-64.

- 684 Xiong, C., Shi, J., Cui, Y., Peng, B., 2017. Snowmelt Pattern Over High-Mountain Asia  
685 Detected From Active and Passive Microwave Remote Sensing. *IEEE Geosci.*  
686 *Remote Sens.* 14, 1096-1100.
- 687 Xu, C.C., Chen, Y.N., Hamid, Y., Tashpolat, T., Chen, Y.P., Ge, H.T., Li, W.H., 2009.  
688 Longterm change of seasonal snow cover and its effects on river runoff in the  
689 Tarim River basin, northwestern China. *Hydrol. Process.* 23 (14), 2045–2055.
- 690 You, Q., Wu, T., Shen, L., Pepin, N., Zhang, L., Jiang, Z., Wu, Z., Kang, S.,  
691 AghaKouchak, A., 2020. Review of snow cover variation over the Tibetan Plateau  
692 and its influence on the broad climate system. *Earth-Sci. Rev.* 201.  
693 <https://doi.org/10.1016/j.earscirev.2019.103043>.
- 694 Yu, Z., Liu, S.R., Wang, J.X., Sun, P.S., Liu, W.G., Hartley, D.S., 2013. Effects of  
695 seasonal snow on the growing season of temperate vegetation in China. *Glob.*  
696 *Change Biol.* 19 (7), 2182–2195.
- 697 Zhang H, Zhang F, Zhang G, Che T, Yan W, Ye M, Ma N, 2019. Ground-based  
698 evaluation of MODIS snow cover product V6 across China: implications for the  
699 selection of NDSI threshold. *Sci. Total. Environ.* 651, 2712–2726.  
700 <https://doi.org/10.1016/j.scitotenv.2018.10.128>.
- 701 Zhang, G., T. Yao, H. Xie, S. Kang, and Y. Lei, 2013, Increased mass over the Tibetan  
702 Plateau: From lakes or glaciers? *Geophys Res Lett*, 40(10), 2125–2130,  
703 <https://doi.org/10.1002/grl.50462>.
- 704 Zhang, G., Xie, H., Yao, T., Li, H., Duan, S.Q., 2014, Quantitative water resources  
705 assessment of Qinghai Lake basin using Snowmelt Runoff Model (SRM). *J.*

706 Hydrol. 519, 976–987.

707 Zhang, Y., Ma, N., 2018. Spatiotemporal variability of snow cover and snow water

708 equivalent in the last three decades over Eurasia. J. Hydrol. 559, 238–251.

709

Journal Pre-proofs

710 **TABLES**711 **Table 1** The attributes and reclassified values of the MOD10C1 (Terra) and

712 MYD10C1 (Aqua) products.

<b>Attributes</b>	<b>Value</b>	<b>Reclassified values in clear index</b>	<b>Reclassified values in fractional snow cover</b>
Fractional snow cover	0–100	/	0–100
Clear index value	0–100	0–100	/
Lake ice	107	100	0
Inland water	237	100	0
Ocean	239	100	0
Cloud obscured water	250	100	0
Data not mapped	253	0	0
Filled	255	0	0

713

714 **Table 2** The RMSE and MAE values of the newly-developed 0.05° and the original

715 0.25° SD products in the different elevation zones

Elevation (m a.s.l.)	RMSE (cm d <sup>-1</sup> )		MAE (cm d <sup>-1</sup> )	
	0.25° SD	0.05° SD	0.25° SD	0.05° SD
	product	product	product	product
1000–2000	0.77	0.76	0.22	0.19
2000–3000	1.98	1.16	1.07	0.54
3000–4000	3.22	2.30	1.78	1.08
4000–4800	1.44	1.29	0.63	0.45
All stations	2.15	1.54	1.12	0.67

716

717 **FIGURES CAPTIONS**

718 **Fig. 1** Spatial domain of the Tibetan Plateau and its 12 basins. The unfilled circles  
719 denote the 92 meteorological stations of the China Meteorological Administration  
720 where the snow depth was observed.

721 **Fig. 2** Flowchart of estimating the cloud-free snow cover probability from the MODIS  
722 Terra snow cover product during 2000–2001.

723 **Fig. 3** Flowchart of estimating the cloud-free snow cover probability from the MODIS  
724 Terra and Aqua snow cover products during 2002–2018.

725 **Fig. 4** Flowchart and the results of the SCP estimation based on the fractional snow  
726 cover and clear index during 1–8 January 2003 using the MODIS Terra and Aqua  
727 products.

728 **Fig. 5** Relationship between the SD and SCP based on 300 grid points during winter  
729 2000 in the (a) western and (b) southeastern TP.

730 **Fig. 6** Flowchart of the spatial downscaling method.

731 **Fig. 7** Flowchart of the temporal downscaling method.

732 **Fig. 8** (a–b) RMSE and (c–d) MAE values of the newly-developed  $0.05^\circ$  and the  
733 original  $0.25^\circ$  SD products when validated against the ground-observed SD data from  
734 92 meteorological stations across the TP.

735 **Fig. 9** Spatial patterns of the (a–b) RMSE and (c–d) MAE of the newly-developed  $0.05^\circ$   
736 and the original  $0.25^\circ$  SD products from the validations against the ground-observed  
737 SD data from 92 meteorological stations across the TP.

738 **Fig. 10** Spatial pattern of the multiyear (2000–2018) mean annual SD from the (a)

739 original 0.25° SD product and (b) newly-developed 0.05° SD product over the TP.

740 **Fig. 11** Spatial pattern of the multiyear (2000–2018) mean monthly SD from September  
741 to February over the TP based on the newly-developed 0.05° and the original 0.25° SD  
742 products.

743 **Fig. 12** Multiyear (2000–2018) mean seasonal cycle of the SD over the TP and its 12  
744 basins based on the newly-developed 0.05° product.

745 **Fig. 13.** The spatial pattern of the (a) linear trends (2000–2018) in annual SD from the  
746 newly-developed 0.05° product and (b) significance test across the Tibetan Plateau. The  
747 trend is regarded as statistically significant when  $p < 0.05$ .

748 **Fig. 14** The interannual variations and the linear trends of the basin-scale (a–l) and the  
749 TP-averaged (m) annual SD during 2000–2018.

750

751 **Author Contributions**

752 **Dajiang Yan:** Conceptualization, Methodology, Formal analysis, Software,

753 Investigation, Resources, Data curation, Writing-original draft, Visualization. **Ning Ma:**

754 Investigation, Formal analysis, Writing-original draft, Funding acquisition. **Yinsheng**

755 **Zhang:** Writing-review & editing, Funding acquisition, Supervision.

756

757

758 **Conflicts of Interest:**

759 No potential conflict of interest was reported by the authors.

760

761

Journal Pre-proofs

762 **Highlights:**

763 ➤ A new spatial-temporal downscaling method to produce a fine-resolution SD

764 product

765 ➤ Using the cloud-free snow cover probability to downscale the coarse SD dataset

766 ➤ Development of a daily 0.05° SD product (2000–2018) for the Tibetan Plateau

767 ➤ The TP-averaged annual SD increased slightly during 2000–2018

768

769